Weierstraß-Institut
für Angewandte Analysis und Stochastik
Leibniz-Institut im Forschungsverbund Berlin e. V.

Preprint ISSN 0946 – 8633

Influence of the carrier reservoir dimensionality on electron-electron scattering in quantum dot materials

Alexander Wilms[1], Peter Mathé[1] , Franz Schulze[2] , Thomas Koprucki[1] ,

Andreas Knorr[2] , Uwe Bandelow[1]

submitted: May 3, 2013

[1] Weierstrass Institute
Mohrenstr. 39
10117 Berlin
Germany
E-Mail: Alexander.Wilms@wias-berlin.de
Peter.Mathe@wias-berlin.de
Thomas.Koprucki@wias-berlin.de
Uwe.Bandelow@wias-berlin.de

[2] Institute for Theoretical Physics
TU Berlin
Hardenbergstr. 36
10623 Berlin
Germany
E-Mail: schulze@physik.tu-berlin.de
Andreas.Knorr@physik.tu-berlin.de

No. 1781

Berlin 2013

2010 *Mathematics Subject Classification.* 81V65, 65C05 .

2008 *Physics and Astronomy Classification Scheme.* 73.21.La, 73.63.Kv.

Key words and phrases. quantum dots, Coulomb scattering, quasi-Monte Carlo.

We wish to acknowledge I. Babushkin, C. Brée, F. Jahnke, J.-E. Kim, K. Lüdge, N. Majer, E. Malic, A. Schliwa, K. Schuh, P. Racec and H.-J. Wünsche for fruitful discussions. For the generation of Sobol sequences used in QMC integration, we used code provided by S. Joe and F. Kuo. This work is supported by Deutsche Forschungsgemeinschaft within the collaborative research center SFB 787 Semiconductor Nanophotonics.

Edited by
Weierstraß-Institut für Angewandte Analysis und Stochastik (WIAS)
Leibniz-Institut im Forschungsverbund Berlin e. V.
Mohrenstraße 39
10117 Berlin
Germany

Fax: +49 30 2044975
E-Mail: preprint@wias-berlin.de
World Wide Web: http://www.wias-berlin.de/

Abstract

We calculated Coulomb scattering rates from quantum dots (QDs) coupled to a 2D carrier reservoir and QDs coupled to a 3D reservoir. For this purpose, we used a microscopic theory in the limit of Born-Markov approximation, in which the numerical evaluation of high dimensional integrals is done via a quasi-Monte Carlo method. Via a comparison of the so determined scattering rates, we investigated the question whether scattering from 2D is generally more efficient than scattering from 3D. In agreement with experimental findings, we did not observe a significant reduction of the scattering efficiency of a QD directly coupled to a 3D reservoir. In turn, we found that 3D scattering benefits from it's additional degree of freedom in the momentum space.

1 Introduction

In the last decades, semiconductor quantum dots (QDs) have been intensively studied due to their high performance in various applications. In particular, for telecom application, e.g. lasers or amplifiers, QD devices have shown promising results, like low threshold current and high temperature stability [1].

Typical QD devices contain dots embedded into a two dimensional carrier reservoir (2DCR), for example quantum well (QW), or wetting layer (WL) like structures [1]. However, the 2DCR is believed to hinder high-speed applications of devices like amplifiers, due to its much slower dynamics compared to the internal dots [2]. Hence, there is an extra effort in growing devices with QD structures directly coupled to the bulklike three dimensional carrier reservoir (3DCR), for example via droplet epitaxy [3, 4], or sub-monolayer deposition [5]. According to Sanguinetti et al. [6], the 2DCR was believed to boost the feeding of the quantum dot states with carriers, enabling ultrafast data transmission. Therefore, the aim of this paper is to answer the question:

Is Coulomb scattering between QD and 2D reservoir generally faster than between QD and bulklike 3D reservoir?

Sanguinetti et al. investigated this fundamental question experimentally [6, 7]. Surprisingly, they could not observe any significant impact of the reservoir dimensionality on QD capture. Here this question will be addressed from the theoretical point of view.

The theoretical investigation of Coulomb scattering in QD-2D systems has attracted much attention [8, 9, 10, 11, 12, 13, 14, 15, 16, 17, 18, 19]. In contrast, only few authors investigated QD-3D systems [20, 21, 22, 23].

One reason might be the high numerical effort that goes along with evaluation of the kinetic Boltzmann equation [24] in such systems. Here, we accomplish this challenge by using a quasi-Monte Carlo (QMC) method [25, 26, 27] for numerical integration.

This paper is structured as follows: after the introduction of the model system, we describe the basic equations. Then, we describe the considered Coulomb-scattering processes. Afterwards the achieved results will be discussed. Our main observation from our calculations is that even though significant differences in particular scattering channels appear, the reservoir dimensionality does not affect the feeding of the QD ground state significantly. This is agreement with the experimental findings of Ref. [7]. A description of the quasi-Monte Carlo method for numerical integration can be found in Appx. A.

2 Model under consideration

2.1 Model system

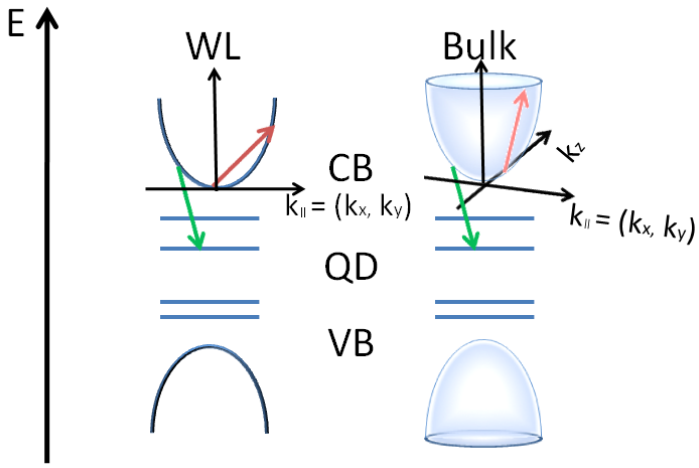

Figure 1: Illustration of the compared systems: system (i): QDs embedded into a 2D carrier reservoir (2DCR), system (ii): QDs embedded into a 3D carrier reservoir (3DCR). For both systems the capture process into a QD excited state (ES) is depicted (cf. Eq. 8).

The impact of the reservoir dimensionality will be investigated by comparing two systems, cf. Fig. 1: (i) QDs embedded into a 2DCR. The dots have one s-like ground state envelope and two degenerate p-like excited states envelopes for each band. We assume independent dot layers in a multilayer device. (ii) the same QDs, but coupled to a 3DCR. In both systems the reservoir is described by a single valence band (VB) and a single conduction band (CB) with parabolic dispersion relations, respectively.

2.1.1 QD wavefunctions

To compare both systems on a fair basis, we assume QDs with the same material parameters and equal wave functions ψ_D in both systems. The QD's compound index D includes the quantum numbers for the band Λ_D, quantum numbers describing the type of the state - for example

s- or p-shell envelope-, the spin σ_D and the QD position $\vec{R}_D$, cf. Ref. [11].

$$\psi_D(\vec{r}) = \hat{\psi}_D(\vec{r}) u_{(\Lambda_l,\sigma)}(\vec{r}) = \xi_D(z)\varphi_D(\vec{r}_{||}) u_{(\Lambda_D,\sigma_D)}(\vec{r}). \tag{1}$$

Here, $u_{(\Lambda_l,\sigma)}(\vec{r})$ denotes a product of Bloch-function times spin part. $\hat{\psi}_D(\vec{r})$ describes the envelope that can be factorized into two parts: (1.) The eigenstates of an infinite barrier $\xi_D(z)$ with an effective height L in growth (z)-direction. (2.) the s- and p-type eigenfunctions of an harmonic oscillator $\varphi_D(\vec{r}_{||})$ in in-plane (x,y)-direction [28, 29, 11]. To distinguish QD ground- (GS) and excited-state (ES), we use the notation $D =$ GS respective $D =$ ES, omitting other quantum numbers.

2.1.2 Reservoir wavefunctions

The envelopes of the 2D reservoir states are also factorizeable into z- and in-plane direction. In z-direction the same wavefunctions $\xi_D(z)$ as for the QD are assumed. The in-plane direction $\varphi_{k_{i,2D}}(\vec{r}_{||})$ is described by 2D orthogonalized plane waves (2D-OPWs) as described in Ref. [11].

The envelopes of the 3D reservoir states [30, 31] are described by 3D-OPWs. Therefore the orthogonalization scheme described in Ref. [11] is applied to full 3D wave-functions. As a result of that, a factorization into z- and in-plane direction is no longer possible.

Reservoir states will be denoted by compound indices k_i. They include band Λ_{k_i} and spin σ_{k_i}, as well as the carrier wavevector $\vec{k}_i$: $k_{i,3D} = (\Lambda_i, \vec{k}_i = (k_x^i, k_y^i, k_z^i), \sigma_i)$ defines the 3D reservoir states and $k_{i,2D} = (\Lambda_i, \vec{k}_i = (k_x^i, k_y^i), \sigma_i, R_z^i)$ defines the 2D ones. Here, also the z-position of the 2D reservoir is a quantum number, as different QD-layers need to be specified. In turn R_z^i does not need to be considered in a single QD-layer.

Unless stated otherwise, different effective masses for QDs (InGaAs) and 3D reservoir (GaAs) are assumed. In turn, we assume equal effective masses for QD and 2D reservoir, cf. Tab. 1(A). This is a suitable approximation in the QD-2D system, as it approximately fits to the situation of QDs grown on a WL. Sanguinetti et al. analyzed a GaAs/ AlGaAs system. However, here we consider an InGaAs/ GaAs system due to it's high importance in recent laser applications. All parameters used in calculations can be found in Appx. D.

2.2 Hamiltonian and Coulomb scattering matrix

In the framework of second quantization the occupation $\rho_a = \langle a_a^\dagger a_a \rangle$ can be expressed in terms of the well known creation/ annihilation operators $a_a^\dagger / a_a$. The compound index "a" defines the set of quantum numbers of the system state $|\psi_a\rangle$, cf. Ref. [24]. We determined the dynamics of a QD state ρ_D via Heisenberg equations of motion [24]. The influence of Coulomb scattering processes are included via a Hamiltonian containing the Coulomb interaction part $H_C = \frac{1}{2}\sum_{abcd} V_{abdc}\ a_a^\dagger a_b^\dagger a_c a_d$ besides the free particle part $H_{0,el} = \sum_m \varepsilon_m a_m^\dagger a_m$. H_C describes a two particle interaction. Particles in the states a and b are created whereas particles in the states c and d are destroyed. The sums run over all system states: The QD states, where the indices have the form of the compound index D, as well as the 2D- or 3D-reservoir states

k_i.
$V_{abdc} = -\int d^3r \int d^3r' \psi_a^*(\vec{r})\psi_b^*(\vec{r'})V(|\vec{r}-\vec{r'}|)\psi_d(\vec{r'})\psi_c(\vec{r})$ is an unscreened Coulomb matrix element. With the notation $\vec{q} = (\vec{q}_{||}, q_z) = (q_x, q_y, q_z)$, and the use of its Fourier representation the Coulomb potential can be expressed as [32]:

$$\begin{aligned} V_{abdc} &= -\delta_{R_z^a,R_z^b}\frac{\delta_{\Lambda_a,\Lambda_c}\delta_{\Lambda_b,\Lambda_d}\delta_{\sigma_a,\sigma_c}\delta_{\sigma_b,\sigma_d}}{A} \\ &\times \sum_{\vec{q}_{||}} \frac{e_0^2}{2\epsilon q_{||}} \int dz \int dz' \xi_a^*(z)\xi_b^*(z')e^{-q_{||}|z-z'|}\xi_d(z')\xi_c(z) \\ &\times \int d^2x\ \varphi_a^*(\vec{x})\varphi_c(\vec{x})\ e^{-\mathbb{i}\vec{q}_{||}\cdot\vec{x}} \int d^2x'\ \varphi_b^*(\vec{x'})\varphi_d(\vec{x'})\ e^{\mathbb{i}\vec{q}_{||}\cdot\vec{x'}}, \end{aligned} \tag{2}$$

to describe the QD-2D sample and

$$\begin{aligned} V_{abdc} &= -\frac{\delta_{\Lambda_a,\Lambda_c}\delta_{\Lambda_b,\Lambda_d}\delta_{\sigma_a,\sigma_c}\delta_{\sigma_b,\sigma_d}}{AL_z} \sum_{\vec{q}} \frac{e_0^2}{\epsilon(q_{||}^2+q_z^2)} \\ &\times \int d^3r\ \hat{\psi}_a^*(\vec{r})\hat{\psi}_c(\vec{r})\ e^{-\mathbb{i}\vec{q}\cdot\vec{r}} \int d^3r'\ \hat{\psi}_b^*(\vec{r'})\hat{\psi}_d(\vec{r'})\ e^{\mathbb{i}\vec{q}\cdot\vec{r'}}, \end{aligned} \tag{3}$$

for the description of the QD-3D sample. Here, A denotes the area of a QD layer which is also the quantization area (2DCR) and L_z is the height (z-direction) of the quantization volume $A \cdot L_z$ (3DCR). As a consequence of the 3D orthogonalization procedure, the in-plane and z-direction overlap integrals in Eq. 3 can not be calculated independently anymore. The Kronecker delta $\delta_{R_z^a,R_z^b}$ in Eq. 2 expresses the assumption that only interactions within one layer are considered. Here, this is justified by a sufficiently large distance of the different QD layers to each other. The further Kronecker-deltas in the numerators of Eqs. 2 and 3 stem from the scalar product of Bloch spin part. They describe spin and band conservation of the scattered particles. The latter one is a typical approximation [32, 11, 24].

The in-plane parts of the 2D Coulomb matrix elements are tabulated in Ref. [33].

3 Relevant scattering processes

Within the limit of Born-Markov approximation, the EOM of the occupation ρ_D in a QD state D can be cast in the form of the quantum Boltzmann equation [11, 24].

$$\begin{aligned} \dot{\rho}_D &= \frac{2\pi}{\hbar} \sum_{a,b,c} W_{Dabc}(W_{Dabc}^* - W_{Dacb}^*) \\ &\quad \Big[\rho_b\rho_c(1-\rho_a)(1-\rho_D) - (1-\rho_b)(1-\rho_c)\rho_a\rho_D\Big] \\ &\quad \times \delta(\varepsilon_D + \varepsilon_a - \varepsilon_b - \varepsilon_c) \qquad (4) \\ &= S_D^{\text{in}}(1-\rho_D) - S_D^{\text{out}}\,\rho_D. \qquad (5) \end{aligned}$$

It describes in- and out-scattering of carriers into the state D in terms of the scattering rates S_D^{in} and S_D^{out}. W_{abcd} denotes screened Coulomb matrix elements, in which we included screening

effects in the static limit of the Lindhard Formula, cf. Refs. [15, 24, 34] and Appx. B. The δ-distribution in Eq. 4 results from the Markov approximation. It describes energy conservation. Equation 4 gives already an impression of the shape of the scattering rates as function of the 2D / 3D carrier density $n_{2D/3D}$ of the reservoir. The rates should exhibit two regimes: First, for lower carrier densities, they should increase with increasing carrier density. This is caused by the factor(s) ρ_i, expressing the increasing number of scattering partners. Second, for higher carrier densities, the rates should decrease due to Pauli blocking, described by the carrier occupation factor(s) $(1-\rho_i)$. The existence of these two regimes was described in Refs. [11, 15].

The triple sum in Eq. 4 runs over all states under consideration, i.e. of the dots $a = D_a$ and 2D or 3D reservoir states ($a = k_a$). In the 3D system this gives rise to the evaluation of up to 8D integrals in $\vec{k}$-space. This is numerically demanding, in particular as $d = 8$ is the efficiency barrier between typical Simpson integration and standard Monte Carlo integration. Therefore we used a Quasi-Monte Carlo method [25, 26] for numerical integration, see Appx. A, which enables an efficient evaluation of the high dimensional scattering rates [31].

We consider a system in quasi equilibrium, thus the occupation probabilities can be approximated by Fermi-distributions $\rho_x = f_x = 1/\left(1 + e^{\frac{1}{k_B T}[\varepsilon_x - \mu_{2D/3D}^{\lambda_x}]}\right)$, cf. [11]. Here, ε_x denotes the energy of the state x, relative to the reservoir band edge, and $\mu_{2D/3D}^{\lambda_x}$ is the chemical potential of the 2D / 3D carrier reservoirs [24]. Furthermore, in quasi equilibrium the related out-scattering rates can be determined via the principle of *detailed balance* $S_D^{\text{out}} = S_D^{\text{in}} \frac{1-f_D}{f_D}$, cf. [16].

The notation of Eqs. 4–11 corresponds to a valence–conduction band picture. For evaluation the electron–hole picture is preferable. Basically, this can be achieved via the substitution $f^{VB} = 1 - f^h$. Then the band index λ_x could stand either for electron band e or hole band h.

It is intuitive to assume that significant differences between the 2D- and 3D-QD scattering rates stem from carrier transitions between QD and reservoir states. In the following we will denote these transitions as subsystem transitions (SSTs). To gain a deeper insight into the different nature of the compared SSTs, we decompose the total scattering rate S_{in}^D into sub-processes [18] and classify them by their number of SSTs:

$$S_{\text{in}}^D = \overbrace{S_{D,\text{rel},1}^{\text{in}}}^{\text{0 SST}} + \overbrace{S_{D,\text{cap}}^{\text{in}} + S_{D,\text{3QD}}^{\text{in}}}^{\text{1 SST}} + \overbrace{S_{D,\text{rel},2}^{\text{in}}}^{\text{2 SSTs}} - \overbrace{S_{D,\text{exch.}}^{\text{in}}}^{\text{not classified}} . \tag{6}$$

The main processes for in-scattering into the QD ground state (GS) are illustrated in Fig. 2. Note that Fig. 2 refers to the electron-hole picture, whereas the following formulas refer to the valence–conduction band picture[1]. The various processes are defined as follows:

3.0.1 Without subsystem transition (0 SSTs), relaxation process 1:

$$\begin{aligned} S_{\text{GS,rel,1}}^{\text{in}} =& \frac{2\pi}{\hbar} \sum_{k_a,k_b,D2} |W_{\text{GS}\,k_a k_b \text{ES}}|^2 f_{k_b} f_{\text{ES}} (1 - f_{k_a}) \\ & \times \delta(\varepsilon_{\text{GS}} + \varepsilon_{k_a} - \varepsilon_{k_b} - \varepsilon_{\text{ES}}), \end{aligned} \tag{7}$$

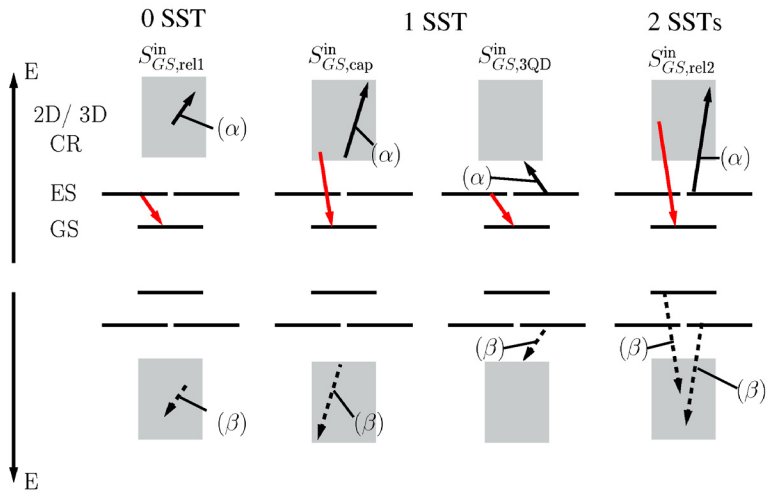

Figure 2: Scheme of the main scattering processes in order of the number of subsystem transitions (SST). Pure electron processes are denoted with (α); mixed processes with (β). The processes are shown in the electron-hole picture, the formulas 7–11 are in a valence-conduction band picture. Not depicted: mixed relaxation process containing the hole ground state in $S^{\text{in}}_{D,\text{3QD}}$.

Here, carriers from the QD excited state (ES) relax into the ground state (GS) and reservoir carriers are scattered to states with higher energy.

3.0.2 With one subsystem transition (1 SST):

(I.) The capture process

$$\begin{aligned} S^{\text{in}}_{D,\text{cap}} =& \frac{2\pi}{\hbar} \sum_{k_a,k_b,k_c} W_{D\,k_a k_b k_c} (W^*_{D\,k_a k_b k_c} - W^*_{D\,k_a k_c k_b}) \\ & \times f_{k_b} f_{k_c} (1 - f_{k_a}) \delta(\varepsilon_{\text{GS}} + \varepsilon_{k_a} - \varepsilon_{k_b} - \varepsilon_{k_c}). \end{aligned} \tag{8}$$

Here, three reservoir states participate, cf. Fig. 2. The capture process describes the filling of the QD states via reservoir carriers by means of a redistribution of reservoir carriers. It includes both direct and exchange interaction. According to Ref. [18], this process determines primarily the long–time dynamics of the QD states.

(II.) The three QD states relaxation process

$$\begin{aligned} S^{\text{in}}_{\text{GS,3QD}} =& \frac{2\pi}{\hbar} \sum_{k_a,D_2,D_3} W_{\text{GS}\,k_a D_2 D_3} (W^*_{\text{GS}\,k_a D_2 D_3} - W^*_{\text{GS}\,k_a D_3 D_2}) \\ & \times f_{D2} f_{D3} (1 - f_{k_a}) \delta(\varepsilon_{\text{GS}} + \varepsilon_{k_a} - \varepsilon_{D_2} - \varepsilon_{D_3}) \\ & + \frac{2\pi}{\hbar} \sum_{k_a,k_b,D_2} |W_{D\,D_2 k_a D_3}|^2 f_{k_a} f_{D_3} (1 - f_{D_2}) \\ & \times \delta(\varepsilon_{\text{GS}} + \varepsilon_{D_2} - \varepsilon_{k_a} - \varepsilon_{D_3}), \end{aligned} \tag{9}$$

where a carrier from a QD excited state relaxes into the GS and a third QD carrier enters the reservoir, see Fig. 2.

3.0.3 With two subsystem transitions (2SSTs), relaxation process 2:

This process describes the in-scattering of a reservoir carrier into the QD-GS by means of the out-scattering of a QD-ES carrier into the reservoir.

$$\begin{aligned} S^{\text{in}}_{\text{GS,rel,2}} =& \frac{2\pi}{\hbar} \sum_{k_a,k_b,D_2} |W_{\text{GS}\,k_a D_2 k_b}|^2 f_{k_b} f_{D_2} (1 - f_{k_a}) \\ & \times \delta(\varepsilon_D + \varepsilon_{k_a} - \varepsilon_{k_b} - \varepsilon_{D_2}) \\ & + \frac{2\pi}{\hbar} \sum_{k_a,k_b,D2} |W_{D\,D_2 k_a k_b}|^2 f_{k_a} f_{k_b} (1 - f_{D_2}) \\ & \times \delta(\varepsilon_{\text{GS}} + \varepsilon_{D_2} - \varepsilon_{k_a} - \varepsilon_{k_b}). \end{aligned} \tag{10}$$

The second term in Eqs. 9and 10 describe the related mixed electron-hole processes, cf. Fig. 2 (β). These terms are only non-zero for carriers in different bands. In Eqs. 7 and 8, these processes are hidden in the sums over all multi-indices, which still contain sums over spin, carrier bands, and other quantum numbers describing the state.

The related exchange term of $S^{\text{in}}_{D,\text{rel,2}}$ and $S^{\text{in}}_{D,\text{rel,2}}$ has the form

$$\begin{aligned} S^{\text{in}}_{\text{GS,exch.}} =& \frac{2\pi}{\hbar} \sum_{k_a,k_b,D_2} \text{Re}\Big[W_{\text{GS}\,k_a D_2 k_b} W^*_{\text{GS}\,k_a k_b D_2} \\ & + W_{\text{GS}\,k_a k_b D_2} W^*_{\text{GS}\,k_a D_2 k_b} \Big] \\ & \times f_{D_2} f_{k_b} (1 - f_{k_a}) \delta(\varepsilon_{\text{GS}} + \varepsilon_{k_a} - \varepsilon_{D_2} - \varepsilon_{k_b}). \end{aligned} \tag{11}$$

It is a mixture of these two processes. Thus, it cannot be classified by the number of subsystem transitions.

A detailed discussion of possible scattering processes and their efficiency in QD-2D structures like here can be found in Ref. [11].

4 Numerical Results

For a comparison of the 2D and 3D scattering rates, the area carrier density n_{2D} $[\text{cm}^{-2}]$ in the 2D reservoir, and the 3D (volume) density n_{3D} $[\text{cm}^{-3}]$ will be related via the well established [35, 36] ratio:

$$n_{3D} = \frac{n_{2D}}{L}. \tag{12}$$

Thus the carrier density in the 3D reservoir is compared with the carrier density in the effective volume $A \cdot L$ of the 2D reservoir. It is emphasized that the effective width L of the 2D reservoir (and the QD) is not arbitrary, but can be calculated if all parameters are known, cf. Ref. [37]. Here the confinement potential of the mesoscopic structures is unknown. Therefore, in this section, we chose a value of $L = 10$ nm which approximately fits to the height of the QD structure assumed here [38]. All figures in this paper are plotted in a way that Eq. 12 holds for equal values of the x-axis. All parameters used for calculations in this section can be found in Tab. 1(A). To investigate the robustness of our findings versus parameter variations, we made parameter studies for the excited state capture process, cf. Appx. C. In this paper, we assume charge neutrality of the reservoirs $n_{2D/3D} = n^e_{2D/3D} = n^h_{2D/3D}$.

In brief, one can summarize the detailed results of this section as follows: The calculated scattering rates show a nonlinear dependency on the carrier densities [11]. In agreement with the experimental findings of Ref. [7], the major scattering rates of the 2D-QD and the 3D-QD systems show similar behavior. Nevertheless, the detailed analysis displays some fundamental differences between the scattering rates, e.g. in the mixed process of $S^{\text{in}}_{D,\text{rel,2}}$. With that, we can illustrate conditions that support significant disparities in some scattering processes, cf. Sec. 4.4. This section is structured as follows: In the beginning the different scattering processes will be characterized, ordered by the number of subsystem transitions (SSTs): First $S^{\text{in}}_{D,\text{rel,1}}$ (Sec. 4.1), followed by $S^{\text{in}}_{D,\text{cap}}$ and $S^{\text{in}}_{D,\text{3QD}}$ (Sec. 4.2). Then $S^{\text{in}}_{D,\text{rel,2}}$ will be discussed (Sec. 4.3).

Then we will discuss under which conditions significant differences could be observable (Sec. 4.4). Finally, we will compare our results with experimental findings (Sec. 4.6).

4.1 $S^{\text{in}}_{D,\text{rel,1}}$ -without subsystem transitions (0 SSTs)

The relaxation rates for 2DCR and 3DCR $S^{\text{in}}_{GS,\text{rel,1}}$ depicted in Fig. 3 show a quite similar behavior. They are nearly equal at low carrier reservoir densities up to about 2 $\times 10^{11}$ cm^{-2}, respective 2 $\times 10^{17}$ cm^{-3}. Above these values Pauli blocking sets in so that the 2D-rate starts to decrease for densities above 6×10^{11} cm^{-2}, whereas the 3D rate still increases up to a density of 12×10^{17} cm^{-3}, cf. Fig. 4.1. In consequence, Fig. 3 shows an up to a factor of about three times higher 3D-rate.

The high similarity of the $S^{\text{in}}_{GS,\text{rel,1}}$–rates before their different decrease with carrier density could be expected, as the absence of subsystem transitions should cause similar Coulomb-matrix elements.

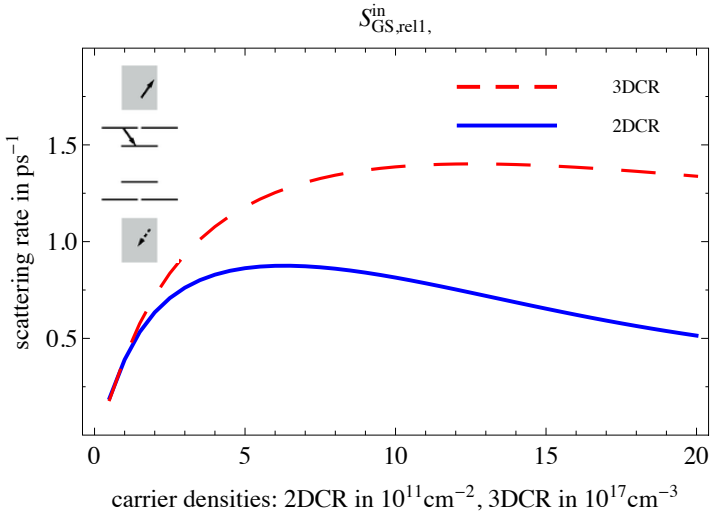

Figure 3: Carrier relaxation rate $S^{\text{in}}_{GS,\text{rel},1}$.

4.2 Processes with one subsystem transition (1 SST)

4.2.1 $S^{\text{in}}_{D,\text{cap}}$ -Capture processes

Figure 4 shows the capture rates into QD's ground (Fig. 4(a)) and excited states (Fig. 4(b)), cf. insets of the figures. The respective 2D- and 3D capture rates are very similar.

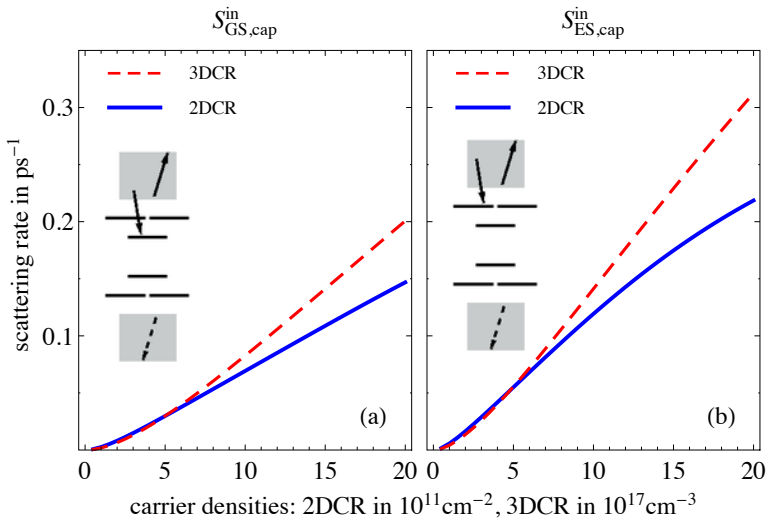

Figure 4: Capture rates: $S^{\text{in}}_{D,\text{cap}}$ into the QD electron ground state $D = GS$ (a), and into the an excited state$D = ES$ (b)

For both processes plotted in Fig. 4 the 2D rate is slightly higher for lower carrier densities. However, for higher densities the 3D-rate exceeds the 2D one. Due to the interplay of many effects, it is difficult to give a strict reason for this minor difference in their behavior. Nevertheless one can

state, that for larger densities, screening effects average over details of Coulomb potential and the increasing density of states (DOS) in the 3D reservoir becomes more and more significant.

The latter argument is also in agreement with the fact, that the flattening of the capture rate due to Pauli-blocking rises earlier for the 2D-rate, than for the 3D-rate, cf. Fig. 4 (b).

These observations remain robust also for different material parameters, see Appx. C. Therefore, we think that the described behavior is typical.

4.2.2 $S^{\text{in}}_{D,\text{3QD}}$ -scattering processes containing three QD states

Similar to the previous findings, the scattering rates $S^{\text{in}}_{GS,\text{3QD}}$, plotted in Fig. 5, resemble each other qualitatively, differ approximately by a factor of 2-3, but have the same order of magnitude. A reason for this relatively large difference of the rates could be found in the different position of the maxima of the 2D and 3D rates, similar to $S^{\text{in}}_{D,\text{rel,1}}$: The 2D rate exceeds its maximum at about $n_{2D} = 8 \times 10^{11}$ cm^{-2}, (which refers to volume density of $n_{2D}/L = 8 \times 10^{17}$ cm^{-3}) whereas the 3D rate increases up to about $n_{3D} = 16 \times 10^{17}$ cm^{-3}. Furthermore the relatively high momentum transfer which takes place in the mixed electron-hole contribution of this process[1] also favors 3D scattering. We will discuss this in more detail in Sec. 4.4.

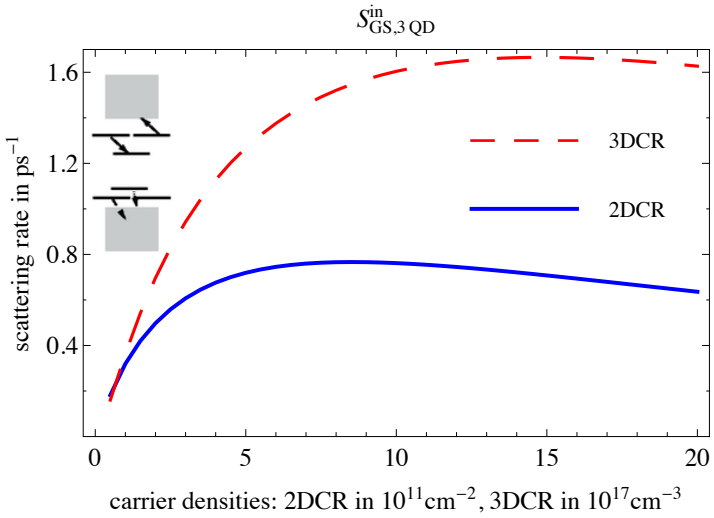

Figure 5: carrier relaxation rate $S^{\text{in}}_{D,\text{3QD}}$

4.3 $S^{\text{in}}_{D,\text{rel,2}}$ -two subsystem transitions (2 SSTs)

The 2D- and 3D-rates $S^{\text{in}}_{GS,\text{rel,2}}$ in Fig. 6 show comparable behavior, though both rates differ significantly already for low carrier densities. This is different compared to the scattering processes previously described. However, also in Fig. 6 the rates are in the same order of magnitude. It is remarkable that here, the rate of the 3D sample is about three times higher than the 2D one

[1] Note that the pure electron contribution to $S^{\text{in}}_{GS,\text{3QD}}$ for the QD-3D sample is exactly zero due to the vanishing density of states.

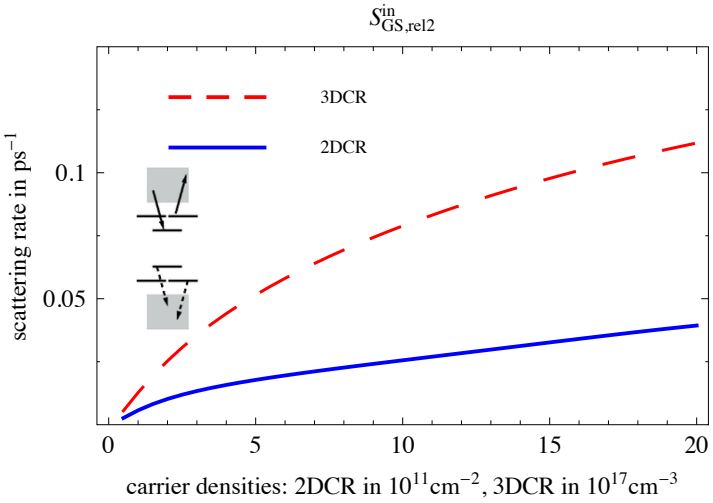

Figure 6: Carrier relaxation rate $S^{\text{in}}_{GS,\text{rel},2}$.

although a maximum is not reached in the plotted density range. This contradicts the intuition. One could expect that the transitions between the 2D reservoir and QD is more effective due to the high overlap of the wave functions in z-direction entering the Coulomb matrix elements Eq. 2.

Of course the higher 3D scattering rate might be supported somehow by the parameter choice of the specific material system, cf. Tab. 1(A), and the Coulomb matrix elements are more than pure overlap integrals of the wave functions. Nevertheless there are also fundamental differences between 2D and 3D scattering, that in principle favor 3D scattering. This will be discussed in the next section.

4.4 Appearance of strong differences in some scattering processes

It is well known that in average the in-plane part of Coulomb matrix elements strongly decreases for increasing momentum transfer, cf. Refs. [11, 33]. As a result of that, scattering processes where a high momentum transfer in in-plane direction takes place, are on average inefficient. Hence, the additional degree of freedom in terms of the z-direction in the 3D reservoir opens the opportunity to increase the scattering efficiency: For given energies of the scattered carriers, the momentum of the reservoir carriers in (x,y)-direction can be lowered by the cost of an increased momentum in z-direction. This effect becomes strongly pronounced e.g. in the mixed process of $S^{\text{in}}_{GS,\text{rel},2}$ depicted in Fig. 7. In Fig. 7 the 2D and 3D scattering rates differ by more than two orders of magnitude. Due to the high effective mass of the holes, the hole reservoir carriers participating in the scattering process have a high momentum of at least $\hbar|\vec{k}_{\text{min}}| = \hbar\sqrt{\frac{2m_h(E_{GS,e}-|E_{GS,h}|)}{\hbar^2}} \approx \hbar\ 1.1\ \text{nm}^{-1}$. As a result of that, scattering in the 2D system is very inefficient. In turn the 3D sample provides still some efficient scattering channels due to its further degree of freedom. We could observe this effect also for other parameter sets in the scattering process $S^{\text{in}}_{GS,\text{3QD}}$, leading to significantly different scattering rates.

Finally the different DOS could also cause strongly different scattering rates. Here, for example,

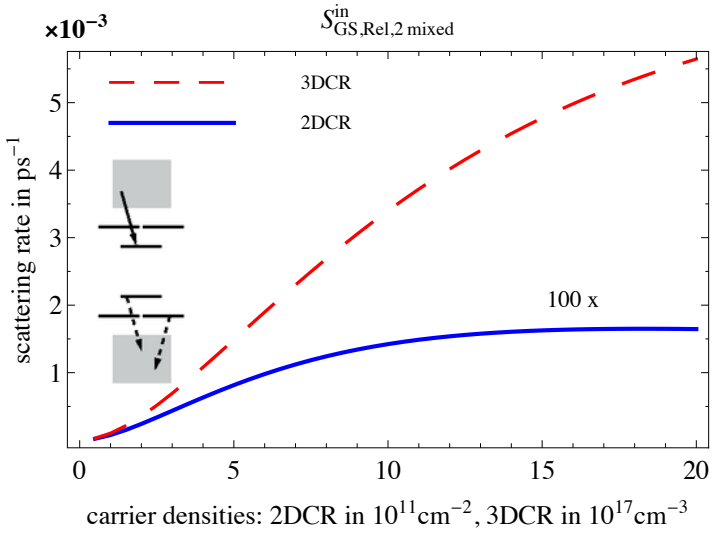

Figure 7: Mixed electron-hole processes of $S^{\text{in}}_{GS,Rel2}$. Note the scaling factor 10^{-3} of the y-axis.

the 3D pure electron rate of $S^{\text{in}}_{GS,\text{3QD}}$ vanishes, whereas the 2D one is small but not zero.

However, we think that appearance of such bottlenecks is supported by the Markovian treatment. Furthermore, we observed that if such a big difference between the 2D and 3D processes appeared in a certain process, its absolute value was significantly smaller compared to other scattering processes. Thus these differences might not be important for device dynamics.

4.5 The relaxation exchange terms

For completeness in Fig. 8 the relaxation exchange terms $S^{\text{in}}_{GS,\text{exch.}}$ are plotted.

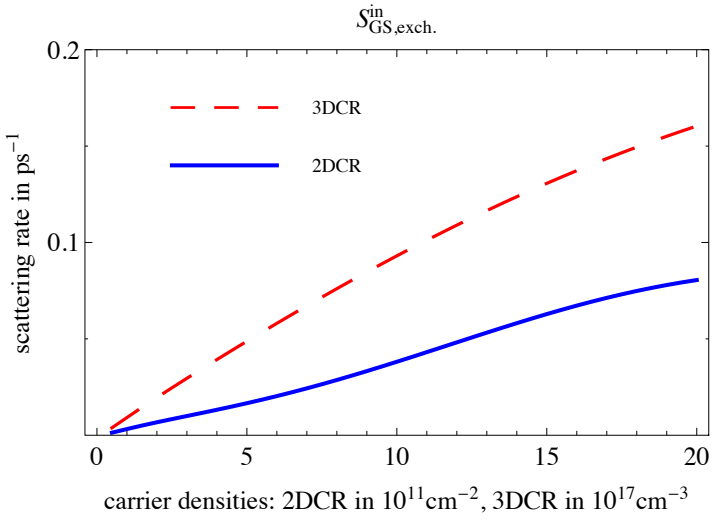

Figure 8: Exchange terms $S^{\text{in}}_{GS,\text{exch.}}$ of the relaxation processes.

The 2D- and 3D-exchange terms show basically the same behavior and are of the same order

of magnitude. However, Fig. 8 suggests an in detail more complex behavior of the 2D-rate than the 3D one.

4.6 Comparison with experiment

Finally we want to compare our results with the experiment of Sanguinetti et al. [7]. They measured the Photoluminescence (PL) rise time τ_r in dependence of the optical excitation power P_{Exc}, cf. Fig. 3 of Ref. [7]. For a full simulation of this experiment a dynamical simulation would be necessary [17, 18]. This is beyond the scope of this paper. Instead, we define the QD-GS filling time τ_{fill}

$$\tau_{\text{fill}} := \frac{1}{2}\Bigg[S^{\text{in}}_{\text{GS,cap}} + S^{\text{in}}_{\text{GS,rel,2,eh}} + 2\left(\frac{1}{\left(S^{\text{in}}_{\text{ES,cap}} + S^{\text{in}}_{\text{ES,rel,2,eh}}\right)} + \frac{1}{\frac{1}{2}\left(S^{\text{in}}_{\text{GS,rel,1}} + S^{\text{in}}_{\text{GS,rel,2,e}} - S^{\text{in}}_{\text{GS,exch.}} + S^{\text{in}}_{\text{GS,3QD}}\right)} \right)^{-1} \Bigg]^{-1}, \tag{13}$$

which describes the average time it takes to fill the QD-GS electron level with reservoir carriers. τ_{fill} is the inverse scattering rate of the direct capture (green), plus twice the rate of the cascading processes (blue), accounting for the two excited states. Equation 13 refers to a device in quasi equilibrium. Furthermore it was assumed that hole scattering is faster [18] than electron scattering so that there are always holes present in the QDs. The suffixes e and eh denote the pure electron and the mixed electron–hole contribution to a certain process. The factor $\frac{1}{2}$ in front of Eq. 13 stems from the spin degeneracy. Figure 9 shows the comparison of the filling time τ_{fill} for the 2D and 3DCR: Both curves basically yield the same dependence on carrier density, thus providing the active support of the experiment. Sanguinetti et al. observed a slightly shorter rise time for the sample with 2DCR. Beyond the general differences in the devices under investigation, this could be caused by the non-uniformly energy spacings of the samples in the experiment. The lower energy spacings in sample with 2DCR favor the Coulomb scattering in this device.

There are several differences in the settings between τ_{fill} (theory) and τ_r (experiment), like the different QDs, the equilibrium assumption in theory which holds not in experiment, and the different plot parameter - the optical excitation power P_{Exc} is measure for the free carrier concentration, but probably not a strict linear one. Beside these differences also the quantities τ_r and τ_{fill} itself are not fully equal: The cascading process in a PL measurement includes more steps than included in Eq. 13, cf. Ref. [39]. Hence the curves in Fig. 9 and Fig. 3 of Ref. [7] are not fully comparable. Nevertheless, the performed comparison of the relative behavior of the respective 2D and 3DCR scattering times is appropriate.

Figure 9 shows that the calculated filling times obey approximately an $\frac{1}{n_{2D/3D}}$ density behavior (besides the highly nonlinear rise of the scattering rates at low carrier densities). This highlights that the bottleneck for the QD filling are the capture processes, with their approximately linear progression for medium and higher densities, cf. Fig. 4. This is in agreement with dynamical simulations [18].

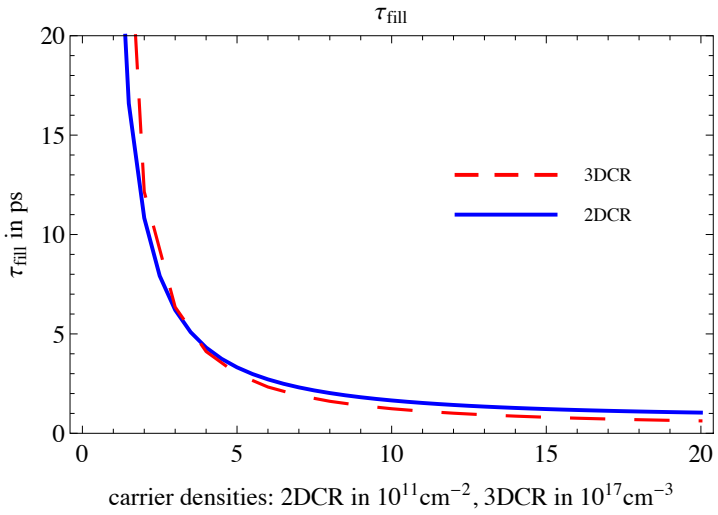

Figure 9: Calculated rise time τ_{fill}.

5 Conclusions

We calculated Coulomb scattering rates from QDs coupled to a 2D carrier reservoir and QDs coupled to a 3D reservoir. Via a comparison of the scattering rates, we investigated the question whether scattering from 2D is generally more efficient than scattering from 3D. For this purpose, we used a microscopic theory in the limit of Born-Markov approximation. The usage of quasi-Monte Carlo method enables a very efficient numerical evaluation of the appearing high dimensional integrals.

We found that although the detailed behavior may depend on specific laser materials, the global behavior of the significant scattering rates is similar. Particularly the rates important for laser long time dynamics are in the same order of magnitude. We could not observe a significant reduction of the scattering efficiency of a QD directly coupled to a 3D reservoir in comparison to a 2D reservoir. This is in agreement with experimental observations [6, 7, 40]. We even found some scattering processes where the related 3D scattering rates are much higher than the 2D ones. This is caused by the additional momentum in z-direction of the 3D reservoir, which could open efficient scattering channels. However, here these scattering processes were insignificant for the feeding of the QD–GS.

A Quasi-Monte Carlo

The equations 8–9 contain integrals in up to five (2D) and eight (3D) dimensions, respectively: By transforming the sums over all reservoir $\vec{k}$-states into integrals over the wavenumber, for example, the pure electron part of the 3DCR capture rate Eq. 8 can be cast into the form[1]

$$\begin{aligned}\int d\vec{x}\; F(\vec{x}) :=& \frac{2\pi}{\hbar} \sum_{\vec{k_a},\vec{k_b},\vec{k_c}} W_D(\vec{k}_a,\vec{k}_b,\vec{k}_c)\Big(2W_D^*(\vec{k}_a,\vec{k}_b,\vec{k}_c) - W_D^*(\vec{k}_a,\vec{k}_c,\vec{k}_b)\Big) \\ & \times f_{k_b} f_{k_c}(1-f_{k_a})\delta(\varepsilon_D + \varepsilon_{k_a} - \varepsilon_{k_b} - \varepsilon_{k_c}) \\ =& \frac{2\pi}{\hbar}\left(\frac{V}{(2\pi)^3}\right)^3 \int d^3k_a \int d^3k_b \int d^3k_c \\ & W_D(\vec{k}_a,\vec{k}_b,\vec{k}_c)\Big(2W_D^*(\vec{k}_a,\vec{k}_b,\vec{k}_c) - W_D^*(\vec{k}_a,\vec{k}_c,\vec{k}_b)\Big) \\ & \times f_{k_b} f_{k_c}(1-f_{k_a})\delta(\varepsilon_D + \varepsilon_{k_a} - \varepsilon_{k_b} - \varepsilon_{k_c}). \end{aligned} \tag{14}$$

Integration in moderate and large dimensions cannot be done by classical quadrature rules because these exhibit the *curse of dimensionality*: If one uses grid based quadrature formulas in say d spatial dimensions, then a mesh size of the order $\varepsilon^{-d/r}$ is required in order to obtain a prescribed accuracy ε, give a smoothness r. This is best possible under sufficient smoothness and using appropriate higher order quadrature. For the integration problem under consideration such smoothness assumptions are not met, and the number of grid points to reach the accuracy ε will be prohibitively large.

In order to motivate the use of quasi-Monte Carlo (QMC) integration rules [25], let us confine ourselves to integration on the d–dimensional unit cube $[0,1)^d$ (for the systems discussed here, this can be achieved by splitting the integrals and performing proper substitutions), and integration with respect to the Lebesgue measure λ_d. Then the integration of a function g can be regarded as computation of the expected value, say $\mathbb{E}g$. In this case the law of large numbers asserts that the sample mean value $\frac{1}{n}\sum_{j=1}^n g(x_j)$ for independently and identically distributed according to λ_d random variables $x_1,\ldots,x_n$ will converge to $\mathbb{E}g$. The error (in root mean square (RMS) sense) behaves like $\left(\mathbb{E}\left|\int g\, d\lambda_d - \frac{1}{n}\sum_{j=1}^n g(x_j)\right|^2\right)^{1/2} \asymp n^{-1/2}$. This rate is dimensionless and indicates the superiority of Monte Carlo integration in higher dimension and under low smoothness assumptions (g just needs to be square integrable).

The crucial observation for QMC integration is the following: In order to have convergence of the sample mean to the expected value it is sufficient for the point set $\{x_1,\ldots,x_n\}$ to be *uniformly distributed on* $[0,1)^d$. Uniformity is measured by the $*$*-discrepancy* $D_n^*(x_1,\ldots,x_n) := \sup_{0<x<1^d} \left|\#\left\{j,\ x_j \in [0,x)\right\}/n - \lambda_d([0,x))\right|$, where the supremum is taken over all rectangular boxes $[0,x)$ anchored at zero. The integration error is then bounded by the *Koksma–*

[1] In (8)–(9), the sum still contains multi-indices, especially the band-index and spin sums are not evaluated on this level. Note, that in Eq. (14) the sum contains just the wavevectors $\vec{k}_i$. The other sums have been evaluated, causing the factor 2 in front of W^*.

Hlawka inequality as

$$\left| \int g \, d\lambda_d - \frac{1}{n} \sum_{j=1}^{n} g(x_j) \right| \leq D_n^*(x_1, \ldots, x_n) V(g).$$

Thus, if the function g has bounded variation $V(g)$ (in the sense of Hardy–Krause [25]) then the error is controlled by the $*$-discrepancy of the used point set. Finding point sets with minimal $*$-discrepancy is a subject of its own. However, the minimum $*$-discrepancy of n points in the cube $[0,1)^d$ is of the order $\log^{d-1}(n)/n$ as $n \to \infty$. Such point sets are called *low discrepancy (LD) point sets*, and these give rise to equi-weight quadrature rules with (almost) dimensionless error bounds. Notice that independent and identically distributed random points have $*$-discrepancy of the order $\sqrt{\log(n)/n}$, which is not competitive to LD points. For further details on constructions and properties of LD point sets we refer to Ref. [25].

The construction of LD points in higher dimension was an issue for a long time, and only recently it became possible to do so by the so–called component-by-component construction. The implementation of LD points which is used here is due to Refs. [26, 27]. Code provided by S. Joe and F. Kuo is used.

As the numerical experiments in 3D exhibit, a number of about 6×10^8 LD points is required to uncover the fine structure of the integrands of the capture rates, regardless of their LD property. This shows that it is hopeless to use classical (grid-based) quadrature rules for the problem at hand. In the 2D case the QMC results are in agreement with earlier results, using grid-based quadrature [11]. The authors also performed some stability experiments to numerically confirm the validity of the obtained rates.

B Screening

In our calculations we included screening in the static limit of the Lindhard Formula [24]. One achieves the relations

$$W_{abcd}^{3D}(\vec{q}) = \frac{V_{abcd}(\vec{q})}{1 + \frac{\kappa_{3D}^2}{|\vec{q}|^2}} \tag{15}$$

for 3D, respective

$$W_{abcd}^{2D}(\vec{q}_{||}) = \frac{V_{abcd}(\vec{q}_{||})}{1 + \frac{\kappa_{2D}}{|\vec{q}_{||}|}} \tag{16}$$

for 2D, containing the screening wavenumber κ (κ_{2D} in 2D and κ_{3D} in 3D). The screening effects can be self consistently derived [34] within the framework of the performed cluster expansion [24].

It is well known [24] that in 3D, there is no possibility to evaluate the screening wave number κ_{3D} via an exact analytic expression. For this purpose one often uses approximations like the

3D Debye-Hückel screening wavenumber. Here, the 3D screening wavenumber (λ denotes the bandindex and ε_{bg} the background permittivity)

$$\kappa_{3D} = \sqrt{\frac{e_0^2}{\epsilon_{bg}} \sum_{\lambda=e,h} \frac{\partial n_{3D}^{\lambda}}{\partial \mu_{3D}^{\lambda}}}. \tag{17}$$

is determined via the approximation

$$\begin{aligned} &\beta\mu_{3D}^{\lambda}(n_{3D}^{\lambda}) \\ &\approx \ln\left[\frac{n_{3D}}{n_0^{\lambda}}\right] + 4.897\ \ln\left[0.045\ \frac{n_{3D}}{n_0^{\lambda}} + 1\right] + 0.133\ \frac{n_{3D}}{n_0^{\lambda}}, \\ &\text{with } n_0^{\lambda} = \frac{1}{4}\left(\frac{2m_{\lambda}k_BT}{\hbar^2\pi}\right)^{3/2}, \end{aligned} \tag{18}$$

by Refs. [41, 42] which is described in Ref. [24]. By calculating the inverse derivative of the Eq. 18, one achieves

$$\frac{\partial n_{3D}^{\lambda}}{\partial \mu_{3D}^{\lambda}}(n_{3D}) = \left(\frac{\partial \mu_{3D}^{\lambda}}{\partial n_{3D}^{\lambda}}\right)^{-1}(n_{3D}^{\lambda}) \tag{19}$$

$$\approx\ 0.133 + \frac{0.220365}{1 + 0.045\ \frac{n_{3D}}{n_0^{\lambda}}} + \frac{n_0^{\lambda}}{n_{3D}}. \tag{20}$$

This can be inserted into Eq. 17. Equation 18 is also used to calculate Fermi distributions in 3D.

C Parameter studies

To affirm the previous findings that the reservoir dimensionality is not significant for the filling of the quantum dot states, parameter studies have been performed. These should answer the questions:

1 Are the previous findings robust versus parameter variations?

2 Are the 2D- and 3D-scattering rates still similar, if one chooses the chemical potential μ as plot parameter?

In this section the discussion is restricted to the capture process into the excited state $S^{\text{in}}_{\text{ES,cap}}$. We chose this process, as it was found [18] to dominate the long time dynamics for the filling of the QD-GS. Majer et al. concluded this from dynamical calculations for a QD-2D sample similar to the one investigated here.

C.1 Robustness concerning parameter variations

To confirm the robustness of the previous findings versus parameter variations, the response of parameter variations will be studied here. Thus, $S^{\text{in}}_{ES,\text{cap}}$ is calculated for 2D and 3D samples

with changed input parameters, see Tab. 1(B) Note that the parameter set Tab. 1(B) represents in particular a significant change of the QD wavefunctions, where the QD level spacing $E_{GS,\lambda} - E_{ES,\lambda}$ enters.

The calculations are done for three different values of the effective height L. This is crucial as this parameter enters the ratio $n_{3D} = \frac{n_{2D}}{L}$ (Eq. 12) and is therefore of high importance. The

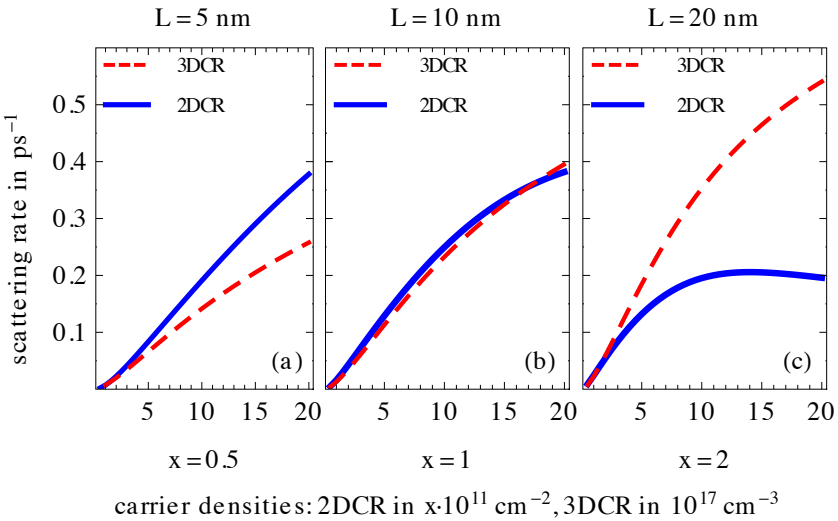

Figure 10: $S^{\text{in}}_{ES,\text{cap}}$ for different parameters, see Tab. 1(B) (a) L = 5 nm , (b) L = 10 nm, (c) L = 20 nm

capture rate Fig. 10(b) shows basically the same behavior as the one in Fig. 4(b). This suggests that the changes in the effective masses and energy spacings do not significantly touch our previous findings. Nevertheless, the fact that the 2D capture rate is here slightly more efficient for nearly the whole density range shows that the detailed behavior is strongly parameter depended. This becomes even more obvious in Fig. 10 (a) and (c). We can see that the parameter L strongly influences which rate is earlier affected by Pauli blocking. In principle this not surprising as for a given value of n_{3D} the related value of $(1 - f_{k,2D}(n_{2D}))$ can be nearly arbitrarily detuned from 1 to 0 by changing L. Therefore L defines whether the related 2D density belongs to the increasing or decreasing regime of the capture rate. Note that for a given structure L is a fixed, well defined parameter. However, the rates depicted in Fig. 10 stay in the same order of magnitude, although we varied L within a wide range. This suggests that the previous findings reflects a typical behavior.

Figure 10 illustrates that the 3D rates increase for increasing L, whereas the 2D rates decrease (note the different scaling factor x in the plot Fig. 10). This seems to be a fundamental difference in the behavior of the 2D and 3D rates. Furthermore, the opposite dependency on L partly compensates the effect of the changed ratio $n_{3D} = \frac{n_{2D}}{L}$ (Eq. 12) of the 2D and 3D carrier densities: (i) Before the Pauli blocking regime is reached the scattering rates are monotonously increasing with increasing carrier density. This is due to the larger amount of scattering partners in the near surrounding of the QDs. (ii) For fixed carrier density n_{3D} Eq. 12 determines the related 2D density n_{2D}. By increasing L also the 2D density n_{2D} is increased. From (i) and (ii) one would expect comparable higher 2D scattering rates for increasing L if one neglects the

explicit dependency of the scattering rates on L.

C.1.1 Hole capture rates

The effective hole masses are about a factor ten times higher than the effective electron masses. Hence, the hole capture rates mirror a strong variation in this parameter. Figure 11 depicts the hole-ES capture rates for the parameter sets Tab. 1(A) (Fig. 11 (*left*)) and 1(B) (Fig. 11 (*right*)).

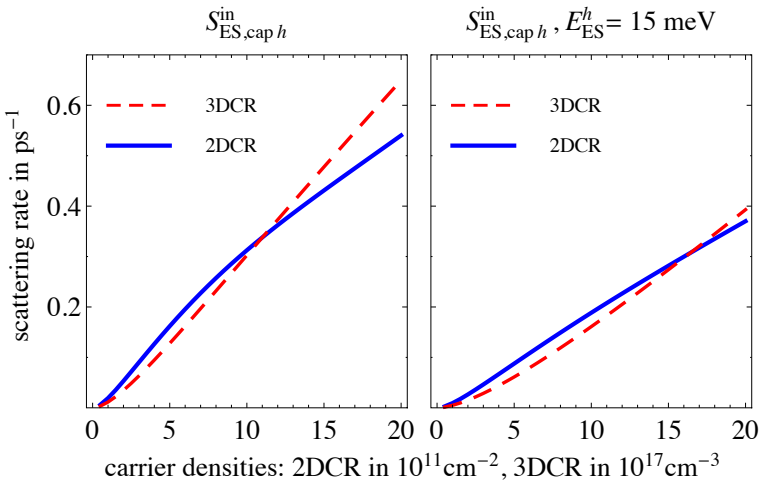

Figure 11: $S^{\text{in}}_{ES,\text{cap}}$ for holes, (*left*): parameters of Tab. 1(A) , (*right*): parameters of Tab. 1(B).

For both parameter sets the rates of the 2D- and 3D sample are very similar. Thus our main observation remains stable for strong variations of the effective mass.

C.1.2 Conclusion of the parameter studies

The scattering rates shown in Fig. 10 and 11 mirror a significant variation of the input parameters. Nevertheless the qualitative behavior is basically the same for the changed parameter sets. This suggests that our previous findings are typical.

C.2 Dependency on the chemical potential

A further useful way to relate the scattering rates is to plot them as a function of the chemical potential μ_e. Accordingly the two samples are compared under the condition of equal chemical potentials for the electrons in the 2D- and the 3D-reservoir respectively ($\mu_e := \mu_e^{\text{2D}} = \mu_e^{\text{3D}}$)[2]. Here the pure electron process make the dominant contribution to the capture rates. Therefore we can skip the mixed electron-hole processes to avoid dealing with deviations from charge neutrality in the respective reservoirs.

[2]One should note, that the 2D reservoir and the 3D reservoir belong to different samples. Thus, this assumption has nothing to do with an equilibrium between the 2D- and 3D-reservoir.

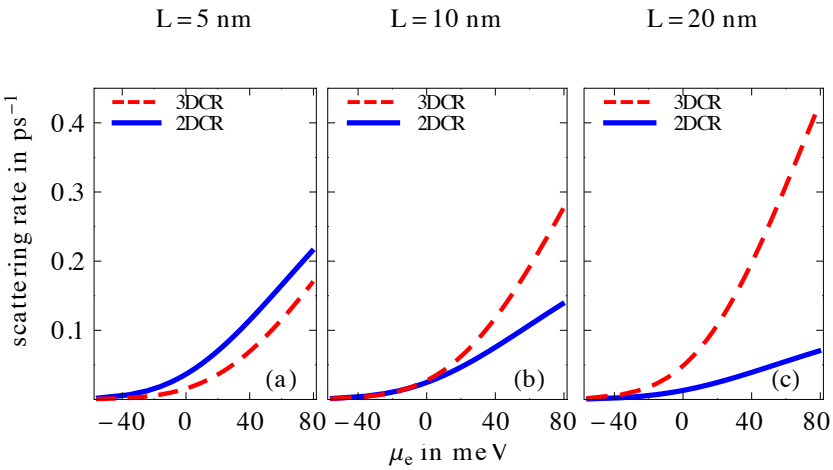

Figure 12: pure CB-electron capture rates as a function of the chemical potential μ_e for different (effective) well width L. Parameter set Tab. 1(A)

The rates plotted in Fig. 12 show a similar behavior to those in Fig. 10. The 2D capture rate decreases with increasing well width L whereas the 3D rate increases. Here, this effect is not compensated by the density ratio Eq. 12, as it is the case in Fig. 10. As a result of that, one can observe a more pronounced difference of the 2D /3D rates for $L = 20$ nm. However, despite this difference, the rates still have the same order of magnitude. This confirms the previous findings of this section, as the main observations remain robust for different ways of comparing the 2D- and 3D-scattering rates.

In contrast to Fig. 10(c), in Fig. 12 the 2D rate does not start to saturate. This confirms that the onset of Pauli blocking in Fig. 10(c) is an parameter effect that is caused by the way of relating the 2D and 3D carrier density.

However, Eq. 12 seems to be the most useful way to relate the scattering rates.

D Parameters

Table 1:
List of Parameters used in calculations. The effective electron (hole) masses m_e (m_{hh}) are used for the QDs and 2DCR, whereas m_{eB} (m_{hhB}) for the 3DCR. The QD sheet density N_{QD} and the layer density density in z-direction [30] N_{Well} enter in the OPW scheme [11]. The QD energies for ground state $\varepsilon_{GS,x}$ and excited state $\varepsilon_{GS,x}$ electrons ($x = e$) and holes ($x = h$) are given with respect to the reservoir band edge. Note that the level spacing $\varepsilon_{ES,\lambda} - \varepsilon_{GS,\lambda}$ enters into the QD wavefunctions.

Symbol	(A) standard Value	(B) varied Value
T	300 K	
m_e	$0.038\ m_0$	
m_{hh}	$0.492\ m_0$	
m_{eB}	$0.067\ m_0$	$0.038\ m_0$
m_{hhB}	$0.5\ m_0$	$0.492\ m_0$
N_{QD}	10^{10} cm^{-2}	
N_{Well}	2×10^5 cm^{-1}	1×10^5 cm^{-1}
L	10 nm	
$\varepsilon_{GS,e}$	-130 meV	-80 meV
$\varepsilon_{ES,e}$	-65 meV	-40 meV
$\varepsilon_{GS,h}$	-35 meV	-30 meV
$\varepsilon_{ES,h}$	-30 meV	-15 meV
ϵ_{bg}	12.5	

References

[1] D. Bimberg, M. Grundmann, and N. N. Ledentsov. *Quantum Dot Heterostructures*. Wiley, New York (1998).

[2] J. Kim, C. Meuer, D. Bimberg, and G. Eisenstein. Applied Physics Letters, **94**, 041112 (2009).

[3] S. Sanguinetti, K. Watanabe, T. T. an M. Gurioli, P. Werner, M. Wakaki, and N. Koguchi. Journal of Crystal Growth, **253**, 71 (2003).

[4] C. Heyn, M. Klingbeil, C. Strelow, A. Stemmann, S. Mendach, and W. Hansen. Nanoscale Research Letters, **5**, 1633 (2010).

[5] N. Ledentsov, D. Bimberg, F. Hopfer, A. Mutig, V. Shchukin, A. Savel'ev, G. Fiol, E. Stock, H. Eisele, M. Dahne, D. Gerthsen, U. Fischer, D. Litvinov, A. Rosenauer, S. Mikhrin, A. Kovsh, N. Zakharov, and P. Werner. Nanoscale Research Letters, **2**, 417 (2007).

[6] S. Sanguinetti, K. Watanabe, T. Tanteno, M. Wakaki, and N. Koguchi. Applied Physics Letters, **81**, 613 (2002).

[7] S. Sanguinetti, M. Gurioli, K. Watanabe, T. Tateno, and N. Koguchi. Semicond. Sci. Technol., **19**, 293 (2004).

[8] A. V. Uskov, F. Adler, H. Schweizer, and M. H. Pilkuhn. J.Appl. Phys., **12**, 7895 (1997).

[9] H. C. Schneider, W. W. Chow, and S. W. Koch. Phys. Rev. B, **66**, 041310 (2002).

[10] H. C. Schneider, W. W. Chow, and S. W. Koch. Phys. Rev. B, **70**, 235308 (2004).

[11] T. Nielsen, P. Gartner, and F. Jahnke. Phys Rev B, **69**, 235314 (2004).

[12] M. Lorke, T. Nielsen, J. Seebeck, P. Gartner, and F. Jahnke. Phys Rev B, **73**, 085324 (2006).

[13] M. Lorke, W. W. Chow, T. R. Nielsen, J. Seebeck, P. Gartner, and F. Jahnke. Phys. Rev. B, **74**, 035334 (2006).

[14] H. H. Nilsson, J.-Z. Zhang, and I. Galbraith. Phys Rev B, **72**, 205331 (2005).

[15] E. Malic, M. J. Bormann, P. Hövel, M. Kuntz, D. Bimberg, A. Knorr, and E. Schöll. IEEE, J. Sel. Topics Quantum Electron., **13**, 1242 (2007).

[16] K. Lüdge and E. Schöll. IEEE Journal of Quantum Electronics, **45**, 1396 (2009).

[17] K. Lüdge and E. Schöll. The European Physical Journal D, **58**, 167 (2010).

[18] N. Majer, K. Lüdge, and E. Schöll. Phys. Rev. B, **82**, 235301 (2010).

[19] T. Koprucki, A. Wilms, A. Knorr, and U. Bandelow. Optical and Quantum Electronics, **42**, 777 (2011).

[20] J. L. Pan. Phys. Rev. B, **49**, 2536 (1994).

[21] J. L. Pan and P. L. Hagelstein. Phys. Rev. B, **49**, 2554 (1994).

[22] A. L. Vartanian. Physica B, **406**, 331 (2011).

[23] R. Wetzler, A. Wacker, and E. Schöll. Journal of Applied Physics, **95**, 7966 (2004).

[24] H. Haug and S. W. Koch. *Quantum Theory of the Optical and Electronic Properties of Semiconductors*. World Scientific, Singapore (2009).

[25] H. Niederreiter. *Random Number Generation and Quasi-Monte Carlo Methods*. SIAM, Philadelphia (1992).

[26] S. Joe and F. Kuo. ACM Trans. Math. Softw., **29**, 49 (2003).

[27] S. Joe and F. Kuo. SIAM Journal on Scientific Computing, **30**, 2635 (2008).

[28] A. Wojs, P. Hawrylak, S. Fafard, and L. Jacak. Phys. Rev. B, **54**, 5604 (1996).

[29] G. Park, O. B. Shchekin, D. L. Huffaker, and D. G. Deppe. Applied Physics Letters, **73**, 3351 (1998).

[30] J. Wolters, M.-R. Dachner, E. Malic, M. Richter, U. Woggon, and A. Knorr. Phys Rev B, **80**, 245401 (2009).

[31] A. Wilms, D. Breddermann, and P. Mathé. Phys. Status Solidi C, **9**, 1278 (2012).
In this publication, a different orthogonalization scheme was used: The in-plane part and the z-part of the 3D reservoir wavefunctions used were orthogonalized separately. the QD height, and For the employed parameters this would lead to smaller 3DCR scattering rates in comparison to the method used here. However, the orthogonalization procedure used in this paper is preferable as eigenvectors and approximated eigenvalues better fit together.

[32] A. Knorr. *Spatial Effects in the Ultrafast Optics and Kinetics of Semiconductors* (1997). Habilitationsschrift. Philipps-Universität Marburg.

[33] T. R. Nielsen. *Carrier-Carrier and Carrier-Phonon Scattering in Self-Assembled Quantum Dots*. Ph.D. thesis, University of Bremen (2005).

[34] E. Verdenhalven, R. Binder, A. Knorr, and E. Malic. Chemical Physics, **413**, 3 (2013).

[35] U. Bandelow, R. Hünlich, and T. Koprucki. IEEE J. Select. Topics Quantum Electron., **9**, 798 (2003).

[36] W. A. Hügel, M. F. Heinrich, and M. Wegener. phys. stat. sol. (b), **221**, 473 (2000).

[37] S. L. Chuang. *Physics of Optoelectronic Devices*. Wiley & Sons, New York (1995).

[38] A. Schliwa, M. Winkelkemper, and D. Bimberg. Phys. Rev. B, **76**, 205324 (2007).

[39] J. Siegert, S. Marcinkevicius, and Q. X. Zhao. Phy. Rev. B, **72**, 085316 (2005).

[40] V. B. Verma, M. J. Stevens, K. L. Silverman, N. L. Dias, A. Garg, J. J. Coleman, and W. P. Mirin. Journal of Applied Physics, **109**, 123112 (2011).

[41] J. Joyce and R. Dixon. Appl. Phys. Lett., **31**, 354 (1977).

[42] V. Aguilera-Navaro, G. Esterez, and A. Kostecki. J. Appl. Phys., **63**, 2848 (1988).